

A novel, magnetically driven convergent Richtmyer–Meshkov platform ^{EP}

Cite as: Phys. Plasmas **27**, 092707 (2020); <https://doi.org/10.1063/5.0013194>

Submitted: 08 May 2020 . Accepted: 14 August 2020 . Published Online: 14 September 2020

P. F. Knapp, M. R. Martin, D. Yager-Elorriaga, A. J. Porwitzky, F. W. Doss ^{id}, G. A. Shipley ^{id}, C. A. Jennings, D. E. Ruiz ^{id}, T. Byvank, C. C. Kuranz, C. E. Myers ^{id}, D. H. Dolan ^{id}, K. Cochrane, M. Schollmeier ^{id}, I. C. Smith, T. R. Mattsson, B. M. Jones, K. Peterson ^{id}, J. Schwarz, R. D. McBride ^{id}, D. G. Flicker, and D. B. Sinars ^{id}

COLLECTIONS

^{EP} This paper was selected as an Editor's Pick



View Online



Export Citation



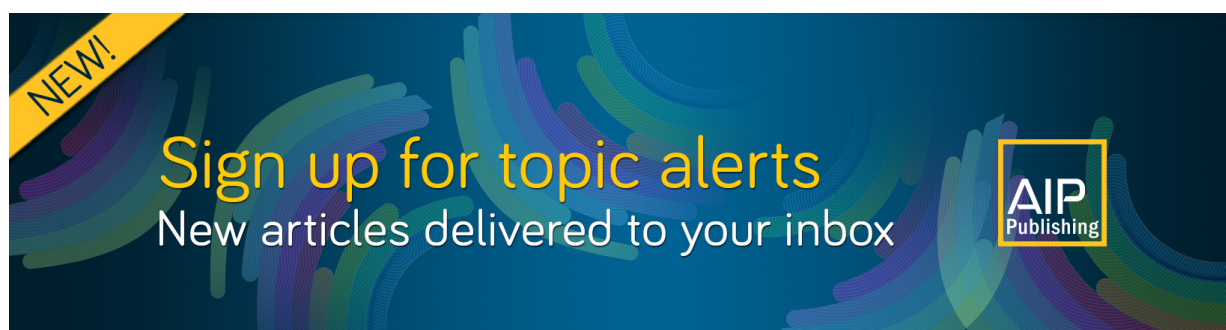
CrossMark

ARTICLES YOU MAY BE INTERESTED IN

[Review of pulsed power-driven high energy density physics research on Z at Sandia](#)
Physics of Plasmas **27**, 070501 (2020); <https://doi.org/10.1063/5.0007476>

[Hot-electron generation at direct-drive ignition-relevant plasma conditions at the National Ignition Facility](#)
Physics of Plasmas **27**, 052706 (2020); <https://doi.org/10.1063/1.5134044>

[Laser-plasma instabilities in long scale-length plasmas relevant to shock-ignition](#)
Physics of Plasmas **27**, 082704 (2020); <https://doi.org/10.1063/5.0010920>



A novel, magnetically driven convergent Richtmyer–Meshkov platform

Cite as: Phys. Plasmas **27**, 092707 (2020); doi: [10.1063/5.0013194](https://doi.org/10.1063/5.0013194)

Submitted: 8 May 2020 · Accepted: 14 August 2020 ·

Published Online: 14 September 2020












View Online



Export Citation



CrossMark

P. F. Knapp,^{1,a)} M. R. Martin,¹ D. Yager-Elorriaga,¹ A. J. Porwitzky,¹ F. W. Doss,²  G. A. Shipley,^{1,2,3}  C. A. Jennings,¹ D. E. Ruiz,¹  T. Byvank,² C. C. Kuranz,⁴ C. E. Myers,¹  D. H. Dolan,¹  K. Cochrane,¹ M. Schollmeier,¹  I. C. Smith,¹ T. R. Mattsson,¹ B. M. Jones,¹ K. Peterson,¹  J. Schwarz,¹ R. D. McBride,⁴  D. G. Flicker,¹ and D. B. Sinars¹ 

AFFILIATIONS

¹Sandia National Laboratories, Albuquerque, New Mexico 87185, USA

²Los Alamos National Laboratory, Los Alamos, New Mexico 87185, USA

³Department of Electrical Engineering, University of New Mexico, Albuquerque, New Mexico 87131, USA

⁴Department of Nuclear Engineering & Radiological Sciences, University of Michigan, Ann Arbor, Michigan 48109, USA

^{a)} Author to whom correspondence should be addressed: pfknapp@sandia.gov

ABSTRACT

In this paper, we introduce a novel experimental platform for the study of the Richtmyer–Meshkov instability in a cylindrically converging geometry using a magnetically driven cylindrical piston. Magnetically driven solid liner implosions are used to launch a shock into a liquid deuterium working fluid and, ultimately, into an on-axis rod with a pre-imposed perturbation. The shock front trajectory is tracked through the working fluid and up to the point of impacting the rod through the use of on axis photonic Doppler velocimetry. This configuration allows for precise characterization of the shock state as it impacts the perturbed rod interface. Monochromatic x-ray radiography is used to measure the post-shock interface evolution and rod density profile. The ALEGRA MHD model is used to simulate the dynamics of the experiment in one dimension. We show that late in time the perturbation growth becomes non-linear as evidenced by the observation of high-order harmonics, up to $n=5$. Two dimensional simulations performed using a combination of the GORGON MHD code and the xRAGE radiation hydrodynamics code suggest that the late time non-linear growth is modified by convergence effects as the bubbles and spikes experience differences in the pressure of the background flow.

Published under license by AIP Publishing. <https://doi.org/10.1063/5.0013194>

I. INTRODUCTION

Hydrodynamic instabilities are ubiquitous processes across much of the physical sciences. They are recognized as key processes responsible for the structures observed in supernova remnants,¹ astrophysical jets,² and nebulae, as well as critical effects required for understanding weather phenomena ranging from storms to regional weather patterns. Additionally, instabilities are a primary degradation mechanism in inertial confinement fusion experiments, being responsible for weaknesses in the confining shell and mixing of material into the hot fuel, both of which will reduce the fuel pressure and, accordingly, the thermonuclear output.³ It is in this context that we are interested in the study of hydro-instabilities in the high energy density (HED) regime.

The Richtmyer–Meshkov (RM) instability develops when a shock crosses an interface with some perturbation present.^{4,5} The interaction of the shock with the perturbation deposits vorticity at the interface, causing the perturbation to grow.⁶ It is distinct from the related

Rayleigh–Taylor (RT) instability which is driven by the sustained acceleration of a light fluid acting on a heavier fluid.⁷ The RT instability is unstable only in this configuration, while the RM instability is unstable as long as there is a density mismatch at the interface, regardless of which fluid is heavier.

Lasers have traditionally been the preferred driver for HED instability experiments due to their availability and flexibility in creating different drive profiles used to isolate individual unstable processes. Planar versions of these experiments use a laser-driven shock to initiate the unstable flow across an interface with a machined perturbation. The relatively low available energy and small spot sizes provided by lasers necessitate that the samples be small and the perturbations correspondingly smaller. Additionally, until recently these experiments were limited to very short timescales ($\lesssim 10$ ns). The advent of the Hohlraum driven shock-shear,^{8,9} Mshock,¹⁰ and RT^{11,12} platforms on the NIF and a direct drive technique on OMEGA EP^{13,14} have

extended the drive times to >20 ns although the spatial scales are still small, stretching the capabilities of existing radiographic diagnostics.

There is also a history of cylindrical laser-driven experiments, where reshock and subsequent mixing have been studied,^{15–17} as well as more recent experiments on OMEGA and the NIF that have studied the growth of azimuthal perturbations in experiments that were hydrodynamically scaled between the two facilities.¹⁸ The cylindrical experiments are limited to very short timescales, $\sim 5 - 7$ ns, on OMEGA and < 1 mm initial target diameter. The most recent experiments on NIF covered a timescale of ~ 20 ns and an initial target scale of ~ 2 mm.

Pulsed power drivers such as the Z machine at Sandia National Laboratories¹⁹ are able to deliver significantly more energy to the target at the expense of power (e.g., Z is able to deliver ~ 2 MJ of magnetic energy to a target, compared to ~ 100 kJ of x-ray drive at the NIF²⁰ and ~ 20 kJ of laser energy at OMEGA²¹). This enhanced energy enables the use of larger targets and larger perturbations, providing higher resolution of the unstable dynamics of interest over time scales comparable to recent NIF experiments. Small modifications to the targets could allow longer timescales to be investigated. Additionally, magnetic drive effectively eliminates the preheat that can be experienced in laser driven platforms, providing better knowledge of the initial conditions at the interface of interest and eliminating the need for pre-heat shields which can significantly complicate target fabrication. Finally, we exploit the natural cylindrical geometry of magnetically driven systems to eliminate edge effects through azimuthal symmetry, obviating the need for tracer layers yet still allowing quantitative local density measurements via Abel inversion.

In what follows, we describe the novel use of the Z pulsed power machine to drive a pure (i.e., no magnetic field in the flow of interest) hydrodynamic, cylindrically convergent RM experiment. In Sec. II, we discuss the general design principles of a magnetically driven convergent RM experiment as well as the specific considerations relevant to these experiments illustrated using 1D ALEGRA calculations.²² In Sec. III, we show the data obtained in these experiments and describe the analysis techniques. Comparisons with 1D ALEGRA simulations as well as 2D simulations provided by a novel linking of the GORGON MHD²³ and xRAGE radiation hydrodynamics²⁴ codes are shown. Finally, in Sec. IV we discuss the results and future applications and extensions of this platform.

II. EXPERIMENTAL DESIGN

The natural geometry for magnetically driven systems is cylindrical as the current flows along a single axis and produces the self-generated Lorentz force that acts radially inward. The Z-machine can drive currents in excess of 20 MA, producing pressures in excess of 100 Mbar. When that current flows through a metallic liner, as shown in Fig. 1(a), the liner will implode, causing the magnetic pressure to increase further accelerating the liner to ≥ 20 km/s, or more. This has been exploited to produce thermonuclear fusion,^{25,26} to study the physics of stagnation,²⁷ and to produce large magnetic fields via flux compression.^{28,29}

Figure 1(a) shows the experimental configuration used for these experiments. A cylindrical beryllium liner is placed at the center of the machine and current is fed to the liner through the final power feed. In this configuration, the return current can is made of Be so as to be transparent to the probing x rays. The Z-Beamlet laser³⁰ is used to

strike two metal targets, which are placed outside the return can, that generate the x-rays used to probe the implosion. The x-rays pass through the load and are reflected by two spherical crystals which focus the x rays and select only a single photon energy. In these experiments, we used the 7.2 keV Co backlighter configuration³¹ which provides $\sim 12 \mu\text{m}$ spatial resolution with a 4×12 mm field of view at the load.

Also shown in Fig. 1(a) is the on-axis photonic Doppler velocimetry (PDV) probe. This probe is similar to that fielded previously²⁷ and is used to measure the imploding shock and liner velocities. The probe can, in principle, measure the shock velocity all the way up until the point that the shock hits the probe. Since the probe outer radius coincides with the rod radius, this is a direct measurement of the shock at the time of impact.

A cross section of the target geometry is shown in Fig. 1(b). The inner radius of the liner is 4.48 mm with a thickness of 0.64 mm. The solid Be rod on-axis has an initial radius of 0.8 mm and a perturbation machined into it with the k-vector in the z-direction (i.e., it is azimuthally symmetric). The mode chosen here has a wavelength $\lambda = 300 \mu\text{m}$ and an amplitude $h_0 = 15 \mu\text{m}$ (peak-to-peak amplitude of $30 \mu\text{m}$), giving $k_z h_0 = 2\pi/\lambda/h_0 = 0.31$, indicating that growth will be in the linear regime initially, but will relatively quickly cross the threshold condition $k_z h = 1$, indicating we should expect non-linear growth. The volume between the liner and rod is filled with liquid deuterium cryogenically cooled to 22 K for an initial density of 167 mg/cm^3 .

The target materials and dimensions were chosen to balance a number of competing factors. The primary consideration is that the 7.2 keV x rays should be able to penetrate the liner and on-axis rod with sufficient contrast and signal to allow observation of the interface as well as the interior of the rod. This necessitates the use of Be as the only transparent conductor that is readily used on Z. Additionally, the working fluid between the rod and liner must be transparent and be a liquid so that it will fill the volume conformally. Cryogenic deuterium is an easy choice for this as its properties are well understood in this regime, routinely used on Z, and satisfy these constraints. The outer diameter and aspect ratio of the liner were chosen to match the energy and pulse length of the driver and balance concerns of stability (which drives to lower aspect ratio) and transparency (which drives to higher aspect ratio). The height of the imploding region is chosen such that any edge waves from the top and bottom surfaces of the implosion will not impact the field of view of the experiment during the times of interest. Finally, the rod diameter sets the shock pressure and the time over which the first shock dynamics evolve. Due to convergence effects, the shock increases in strength as a function of radius. We desire that the rod be melted by the shock so that strength effects are minimized. This sets a maximum radius, above which the shock is too weak to melt the Be. We also require that we have > 10 ns to observe the first shock dynamics, which sets a minimum radius. These constraints allowed us to arrive at the present design; however, there are many other configurations that could produce a satisfactory experiment. The options are further expanded if a significantly higher photon energy backlighter is available as this allows a greater variety of material choices.

A. Shock Dynamics

In the experiments reported here, we use the imploding liner as a piston to drive a strong, converging shock into an on-axis target. The

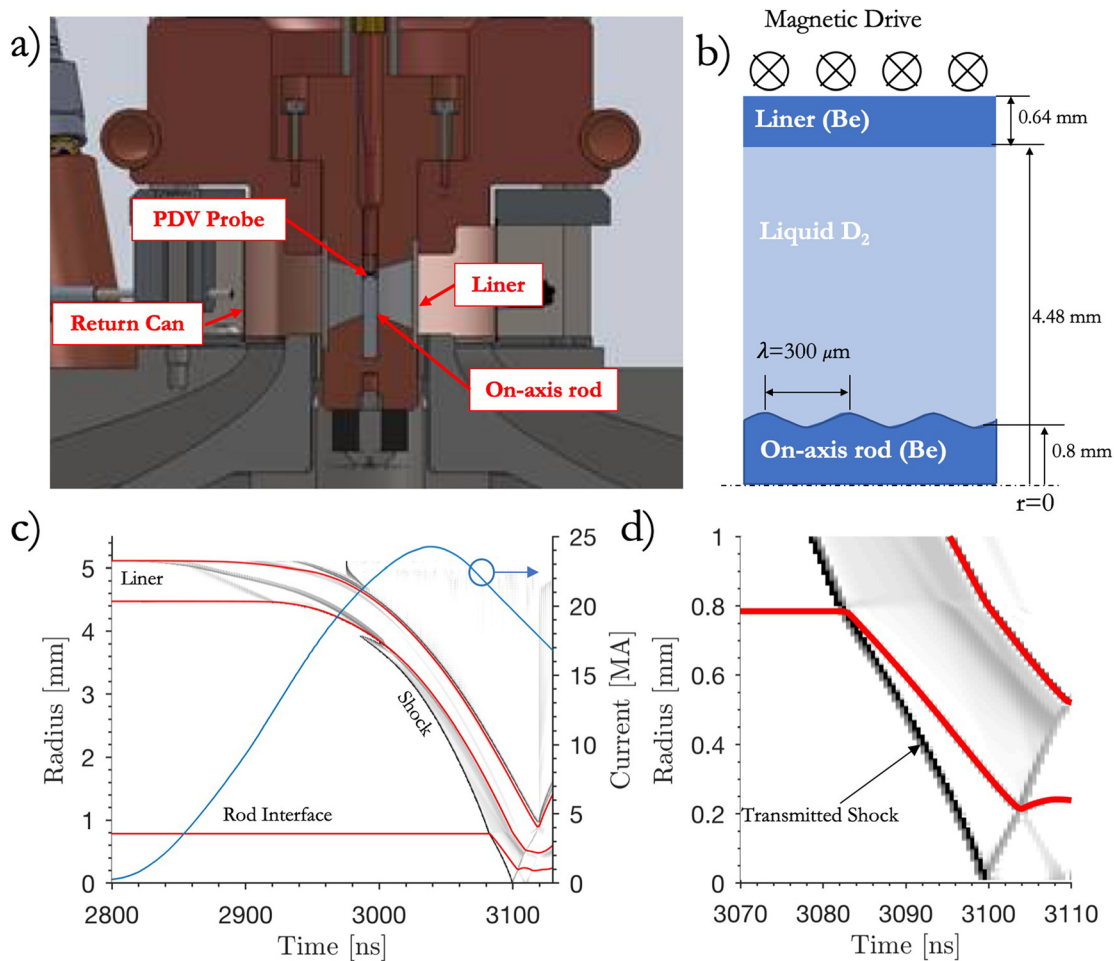


FIG. 1. (a) Cross section view of the load region and the target showing the return current can (anode), liner (cathode), PDV probe, and the on-axis solid rod. (b) Schematic of the target geometry. The axis of symmetry is at $r = 0$. (c) Radius-time plot (on machine time) showing the implosion of the liner, driving a strong shock into the rod. Material interfaces are shown in red. The load current is shown in blue. (d) Close up view of (c) showing the interaction of the shock with the rod. The constant velocity motion of the rod and the transmitted shock are clearly visible as well as the re-shock occurring at $t \approx 3105$ ns. The greyscale image in (c) and (d) is $\propto \nabla P/P$, meant only to highlight the location of the shocks.

liquid deuterium acts as a working fluid, transmitting the shock from the imploding liner to the on-axis rod. Figure 1(c) shows the dynamics of the implosion from a 1D ALEGRA simulation. ALEGRA is used to model these experiments due to its demonstrated capability to accurately simulate magnetically driven flier plates and liners.^{27,32–35} For these simulations, we use tabulated Sesame equations of state³⁶ and electrical conductivities based on Lee-More-Desjarlais (LMD) and Density Functional Theory (DFT) models.^{37–40} The gradient of the material pressure normalized to the material pressure is plotted, allowing easy observation of the movement of shocks in the system. The interfaces are plotted as red lines. The magnetic pressure on the exterior of the liner increases as the square of the current, eventually becoming great enough to implode the liner, driving a shock in the deuterium. The shock increases in strength due to convergence effects⁴¹ and is constantly supported by the imploding liner behind it.

Figure 1(d) shows a close up of the interaction of the shock with the rod. When the shock hits the rod, the interface is impulsively

accelerated to a roughly constant velocity of ~ 20 km/s, and a strong shock is transmitted into the beryllium. The shock then reflects off the axis and strikes the beryllium/deuterium interface for the second time. There is a transit time of ~ 17 ns in between the first shock and re-shock, during which time the rod interface implodes with nearly constant velocity and the RM instability causes the initial perturbation to grow. During this phase, the interface experiences a nonzero radial acceleration that leads to a small growth amplification due to the RT instability. However, using the 1D calculation to estimate the time over which the interface is RT unstable, we find that we would expect a growth factor of three, while the RM growth factor is expected to be eight over the same period. Therefore, we treat the dynamics during this first-shock phase as being dominated by the RM instability. After reshock the situation gets significantly more complicated: multiple reflected shock waves are seen reverberating in the compressed rod and deuterium regions. More specifically, for a brief ~ 2 ns period after reshock, there is a violent phase inversion of the interface perturbation,

which is primarily dominated by the RM instability. In the subsequent phase $\sim 2 - 8$ ns after reshock, a small yet nonzero inward acceleration of the interface causes the surface perturbation to rapidly grow due to the RT instability. In the experiments reported in this paper, we focus on the relatively simpler growth of the perturbation during the first-shock phase; i.e., between 3085 and 3106 ns in Fig. 1(d).

B. Magnetic Diffusion

In order to drive purely hydrodynamic instability growth, we must ensure that the magnetic field used to drive the liner is sufficiently excluded from the region of the shock interaction so that it does not have an effect on the dynamics. This corresponds to the condition that $\beta \gg 1$, where $\beta \equiv P_{\text{kin}}/P_{\text{mag}}$ is the ratio of the kinetic to magnetic pressure in the region and times of interest. Satisfying this condition ensures that any magnetic field that does diffuse into the region of the rod will not perturb the dynamics, thus making sure this platform is suitable for hydrodynamic instability studies.

Current initially flows on the exterior of the liner and, as it increases, the magnetic field will begin to diffuse into the bulk liner material. As the current increases further, the magnetic field will exert sufficient pressure on the liner to move it. This can result in the formation of a shock inside the liner. When this occurs, the bulk of the liner material will move once the shock breaks out of the inner surface. In general, the magnetic field diffusion front will closely follow the shock in the liner. Therefore, minimizing or eliminating the shock entirely in the liner will help to limit the diffusion of drive field into the interior of the liner. This can be accomplished by tailoring the current pulse amplitude in time or choosing the liner thickness such that the pressure waves launched at the drive surface coalesce at a radius that is smaller than the inner radius of the liner, preventing the formation of a shock inside the liner.³⁵

For these experiments, we chose to operate Z in long-pulse mode, with a current rise time of ~ 300 ns, which helps to adiabatically compress the liner and hold off the subsequent magnetic field diffusion that rapidly occurs in shock-melted liners. Figure 2 shows the

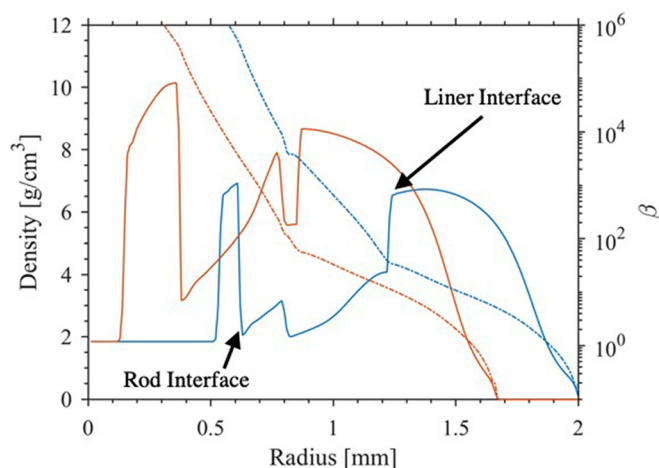


FIG. 2. Plot of the material density (solid lines) and plasma β (dashed lines) at $t = 3080$ ns (blue) and $t = 3088$ ns (orange) showing that the rod is not significantly affected by the drive magnetic field.

evolution of the material density and β as a function of radius at two different times after the shock has impacted the rod as predicted using 1D ALEGRA simulations. At all times, $\beta \gtrsim 10^5$ at the interface between the deuterium and the rod and ~ 100 at the deuterium/liner interface. The location where $\beta \leq 1$ is always located on the outskirts of the liner material. Barring anomalous magnetic diffusion that is not captured in the code, which would have to be incorrect by several orders of magnitude, we are confident that the drive field is sufficiently excluded from the region surrounding the rod so as to make this a purely hydrodynamic experiment.

It is worth noting that as the parameters of the experiment are varied, this question should be revisited. If, for example, the initial liner diameter is made substantially smaller, this could change the distribution of magnetic field, and pulse shaping could be required to mitigate field diffusion into the region of interest.

III. DATA AND ANALYSIS

As stated, radiography is the primary diagnostic used to measure the evolution of the perturbation. Figure 3(a) shows an example radiograph obtained on experiment z3244. The radiograph has been corrected for transmission and is displayed in units of optical depth, $\tau_\nu = -\ln(T_x)$, where T_x is the measured transmission and $\tau_\nu = \rho \ell \kappa_\nu$ is the optical depth. With knowledge of the opacity κ_ν , this information can be used to determine the local material density by Abel inversion. A few important features are apparent in the radiograph in Fig. 3(a). We see the inner surface of the liner at a radius of approximately 0.5 mm, and we can see the modulation of the liner density by the magneto-Rayleigh Taylor instability. These modulations produce variations in optical depth at the interior of the liner which lie overtop of the rod, highlighted by the red box. This instability is the chief deleterious effect that must be controlled in order to produce a 1D cylindrical interaction with the rod. If this instability grows too far, it can imprint on the rod and complicate the dynamics. Figure 3(b) shows a close up of the rod from the same radiograph. The perturbation on the outside of the rod is clearly visible, as well as the shock inside the rod which is at a radius of $\sim 400 \mu\text{m}$ in this image.

Figure 4 shows the rod density obtained by Abel inversion of all five radiographs acquired in this campaign. This progression clearly shows the evolution of the perturbation and the propagation of the shock inside the rod. Figure 4(a) was obtained just prior to the impact of the shock with the rod, providing an *in situ* image of the initial condition. Analysis of this image shows that the rod has not been perturbed from its initial state. The wavelength and amplitude match the design specifications, and there are no observable effects of parasitic current flow in the rod (e.g., premature expansion or surface modulations), thus proving the lack of deleterious pre-heating effects commonly observed in other platforms. Stepping forward in time we see the perturbation amplitude grows and the shock front converges toward the axis. In Fig. 4(e), the shock has reflected off the axis and is propagating back outward toward the interface although it has not impacted the interface yet. In each of the frames, it is clear that the shock front is remarkably straight over the entire 2 mm field of view used for analysis, and no curvature of the perturbed interface is observed. These observations indicate that, apart from the perturbation growth itself, the shock and compression dynamics are highly 1D, as expected.

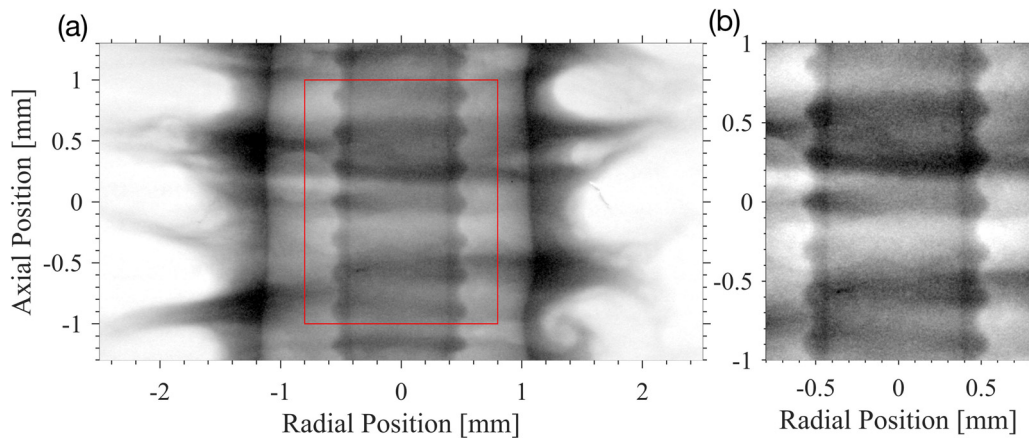


FIG. 3. (a) Full radiograph (shown in optical depth) from z3244. The liner inner surface is seen at $r \approx 1$ mm with the magneto Rayleigh–Taylor instability evident on the exterior. The perturbed rod is visible in the center of the image. (b) Close-up view of the rod showing the perturbation and the location of the shock inside the rod.

Because we can only measure the density of the beryllium at each point in time represented by the radiographs, and not all of the relevant flow variables, we must convince ourselves that the 1D simulations adequately reflect the experimental dynamics in order to fully analyze the instability growth. Figure 5 shows the 1D simulated in-flight dynamics compared to the measured PDV data. Figure 5(a) shows the velocity of both the liner (dashed black line) and the shock (solid black line) from the simulation compared to the measured shock (yellow) and liner (orange) velocities. The agreement is generally quite good, apart from a small region in time around 3000 ns. Figure 5(b) shows the same data, integrated in time to give the shock and liner trajectories compared to 1D. The PDV system only returns useful data from a portion of the trajectory, but it is long enough to confirm that the shock is being launched as predicted and is in agreement with the 1D simulations up to a convergence ratio of ~ 2 . To validate the dynamics further, we must examine the radiographs in more detail and compare them to the density profiles predicted by 1D.

Figure 6 compares lineouts of the measured density profile from the images obtained on experiment z3244 at $t_1 = 3095$ ns(a) and $t_2 = 3104$ ns(b) to lineouts from a post-shot 1D simulation driven with the measured load current at the corresponding times. The experimental data are shown in black, the simulated Be density profile is shown in blue, and the simulated deuterium density profile is shown in orange. The materials are plotted separately because the deuterium is not observable in the experiment due to its low opacity to the 7.2 keV radiography probe x rays. The experimental lineouts are taken by averaging the Abel inverted density profiles over a height of ~ 1 mm to reduce noise. It is readily seen that at both times the inner surface of the liner, the outer surface of the rod and the location of the shock in the rod are all reproduced very accurately by the simulation. The density of the outer surface of the liner is not accurately captured, but this is due to the higher dimensional structures associated with the MRT instability on the drive surface of the liner. It is also worth noting that the rod/deuterium interface is sloped in the radial direction in the

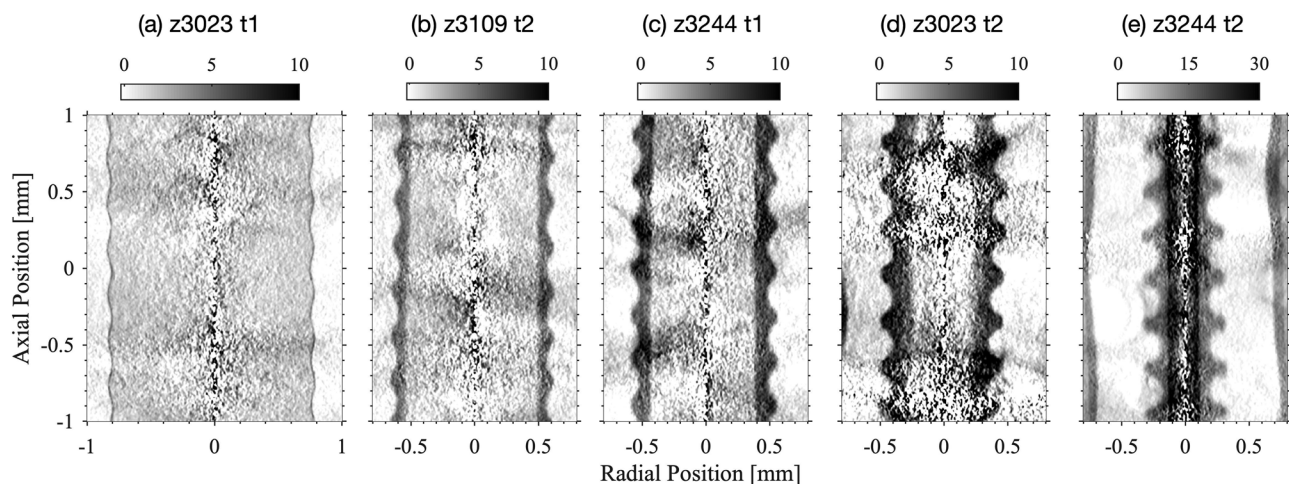


FIG. 4. Be rod densities obtained by Abel inversion of the radiographic data at times (a) z3023 $t_1 = 3081$ ns, (b) z3190 $t_2 = 3093$ ns, (c) z3244 $t_1 = 3095$ ns, (d) z3023 $t_2 = 3099$ ns, and (e) z3244 $t_2 = 3104$ ns. The colorbars above each image show the density in g/cm^3 .

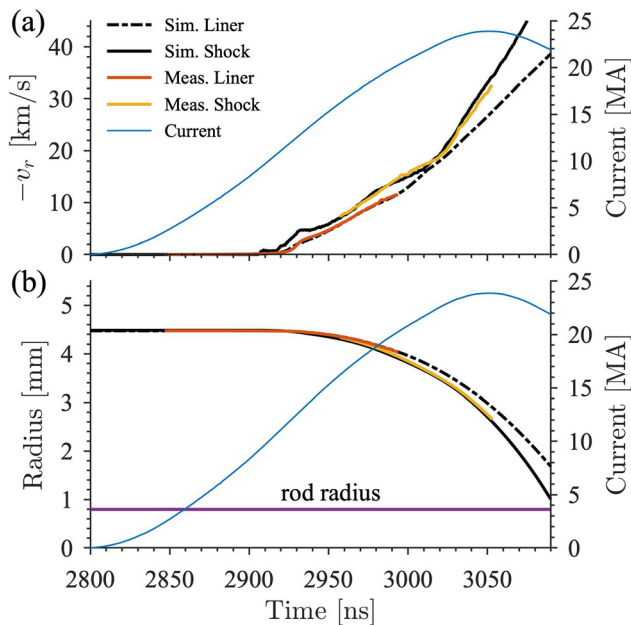


FIG. 5. Comparison of simulated and measured inflight trajectories for the liner and shock. (a) In flight shock (yellow) and liner (orange) velocities measured by PDV compared with simulation (black solid and dashed lines, respectively). The drive current is shown for reference in blue. (b) Position as a function of time for the shock (yellow) and liner (orange) obtained by integration of the velocities compared with simulation. The dashed black line shows the location of the rod.

experimental data, while it is sharp in the simulation. This is simply because the experimental lineouts are averaged over the perturbation which introduces a variation in the location of the interface as a function of height which is not captured in the 1D simulation. It is apparent that this effect is exacerbated at late times when the perturbation is

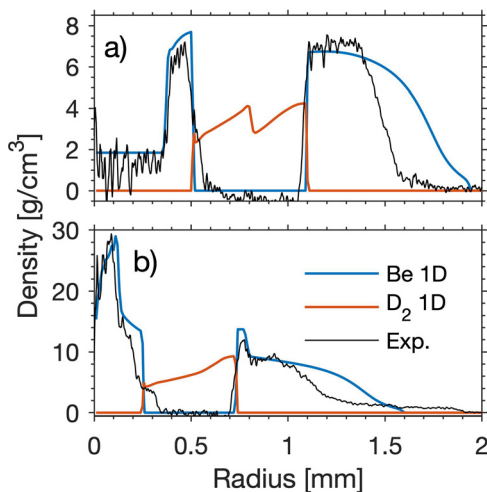


FIG. 6. Density lineouts from experiments z3244 t_1 (a) and t_2 (b) shown in black. Density profiles from the 1D simulation at the corresponding times are also shown in blue (Be) and orange (D_2).

larger. Despite this complication, the agreement is excellent and representative of the agreement between the data and simulation at all times. The agreement between the Be densities and locations of multiple interfaces strongly suggests that 1D simulations are sufficiently accurate to constrain quantities that are not directly measurable, such as the deuterium density which is needed to determine the Atwood number.

Using a density tracking algorithm, we are able to track the contour of the perturbation on each image shown in Fig. 4 for the left and right sides of the image. An example of this is shown in Fig. 7(a) for the right side of the rod in the first image taken on z3244 [corresponding to Fig. 4(c)]. The location of the shock in the rod is also shown as the dashed red line in this image. These contours allow us to derive the perturbation amplitude and interface position as a function of time. The location of the interface is determined by finding the radial position at which the bubbles and spikes occupy equal volume. The bubble and spike volumes are determined as

$$V_{B,S} = \pi \int_H |r_{B,S}^2 - r_{int}^2| dz, \quad (1)$$

where $r_{B,S}$ is the position of the bubble (spike) as a function of height and r_{int} is the position of the interface, which is varied until $V_B = V_S$, shown in Fig. 7(b). This metric for determining the interface position is found to be in excellent agreement with the 1D simulations.

With this information we can then determine the interface position as a function of time and the growth of the perturbation. We find that the measured interface velocity is $v_i = 19.5 \pm 2$ km/s and the transmitted shock velocity in the rod is $v_{S,T} = 26.7 \pm 2$ km/s. Examining the 1D simulation results, we find that the Atwood number is constant in time and has a value of $A_N = (\rho_{Be} - \rho_D)/(\rho_{Be} + \rho_D) = 0.53$, and the reflected shock in the deuterium region has a velocity in the lab frame of $v_{S,R} = 0$ km/s, i.e., it is a standing shock. This information allows us to compare the measured growth to analytic predictions. Lombardini *et al.* have developed a linear theory for the RM instability that takes into account convergence effects as well as the impact of the proximity of the reflected and transmitted shocks to the interface.⁴²

In order to appropriately compare with theory, we must account for the compression of the perturbation due to the passage of the shock. Generally, RM theory uses this *post-shock* amplitude as the initial condition for calculations. We do not have a radiograph of this phase, and the compression occurs while the interface is being accelerated to its terminal post-shock velocity, so the measurements of the shock and interface velocities cannot be used to estimate it either. Using the 1D simulation, we determined how far the interface is displaced by the time the shock reaches the *lowest* point in the perturbation (i.e., by the time the shock has traveled $15 \mu\text{m}$). In this time, the interface has moved $5 \mu\text{m}$. We then assume that the *highest* point in the perturbation has moved twice as far, e.g., $10 \mu\text{m}$, because it has been moving for twice as long. This gives a *post-shock* perturbation amplitude of $h_{PS} = 10 \mu\text{m}$, a compression factor of $\sim 1.5\times$, which takes approximately 0.5 ns to occur.

Figure 8 shows the data points compared with the cylindrical theory using h_{PS} as the initial amplitude, plotted against the normalized interface displacement $k_z \delta r$, where $k_z = 2\pi/\lambda \simeq 21 \text{ mm}^{-1}$. The shaded bands around the lines denote the theory predictions within the confidence interval for the measured interface velocity. We find

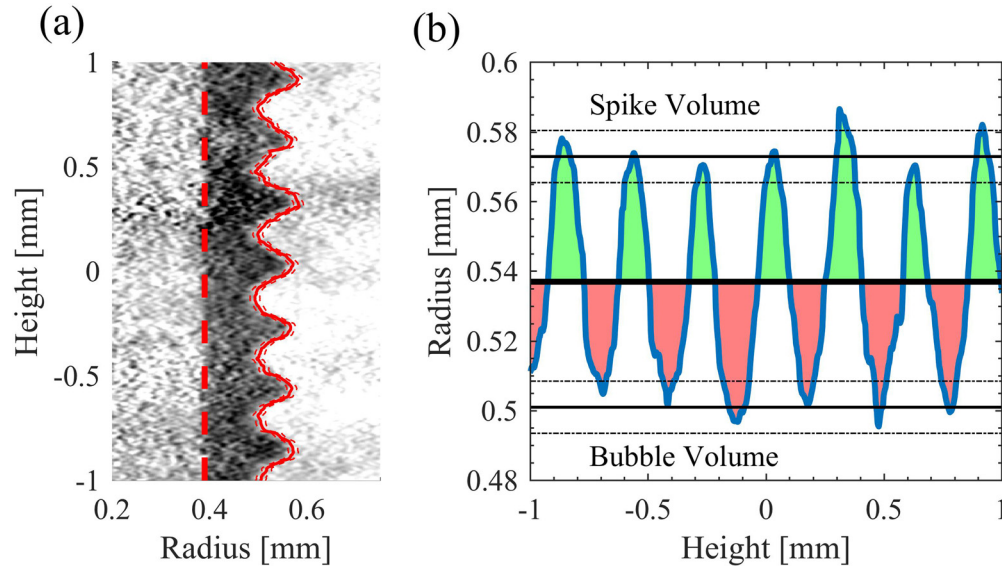


FIG. 7. (a) Right side of the rod from the first image taken on z3244 showing the perturbation contour (solid red) and the shock position (vertical dashed red). (b) Contour plotted with the interface position (bold black line) shown equally dividing the bubble (red) and spike (green) volumes. The average perturbation amplitude is denoted by the thin black lines with uncertainty denoted by the thin dashed black lines.

that the cylindrical theory agrees quite well with the measurement initially, then seems to lie between the later two data points, making it seem as though the perturbation is briefly growing faster than linear theory predicts. This is, in particular, surprising since, for the last two measurements, the instability is clearly in the nonlinear regime with $k_z h > 1$. It is also worth noting that weakly nonlinear theories suggest that the RM instability should slow down once it enters the nonlinear regime.^{43,44} In contrast, these measurements suggest that the

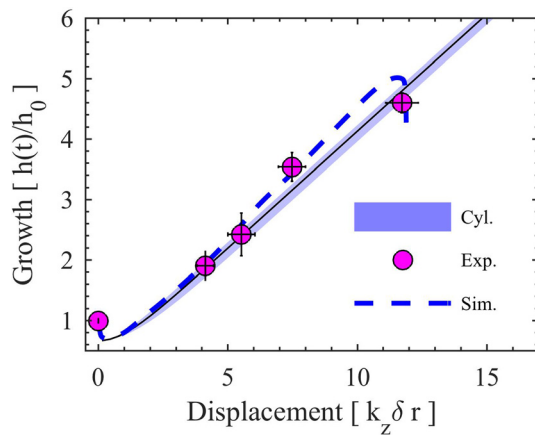


FIG. 8. Growth of the seeded perturbation as a function of the dimensionless displacement of the interface, $k_z \delta r$. Here $k_z = 2\pi/\lambda$ is the mode wavenumber and δr is the displacement of the interface from its initial position. $k_z \delta r = 0$ is the point when the shock first hits the interface. Predictions of the growth using the theory from Lombardini *et al.*⁴² is plotted using the Atwood number determined from simulation, $A_N = 0.53$, as the shaded region. The widths of the shaded regions are determined by the confidence interval for the measured interface velocity. Results from the 2D simulation are shown as the dashed blue line.

perturbation is briefly growing faster than what linear theory predicts. This discrepancy may be in part due to the fact that a constant interface velocity is used or to the fact that the RT contribution is not included in this analysis.

Upon examination of the contours from the last data point, it is apparent that the growth has become nonlinear and there is obvious asymmetry between the bubble and spike regions. Despite the agreement with 1D simulation, the metric used to determine the interface position may be suspect due to the asymmetric shapes of the bubbles and spikes. Additionally, the amplitude of the mode is now a significant fraction of the rod's radius, implying that convergence effects should be strongly modifying the evolution of the perturbation.

Figure 9 shows the Fourier transform of the contours derived from both images obtained on z3244. The earlier image is shown in blue and the later image, which corresponds to the latest observed data point, in orange. The large peak centered at $k_z \simeq 21 \text{ mm}^{-1}$ corresponds to the seeded perturbation and defines the first harmonic ($n = 1$). Already in the earlier data we see the appearance of energy in the second harmonic ($n = 2$), but nothing noticeable above the noise at higher wavenumbers. At the later time, however, we see energy in all modes up to $n = 5$ indicating that the mode growth is nonlinear. Although it is not shown, the contour corresponding to z3023 t_2 [Fig. 4(d)] also shows the presence of higher modes at significant amplitudes, even though the total growth seems to be greater than that predicted by linear theory. At this time, the perturbation growth satisfies $k_z h > 1$. Therefore, the perturbation growth has entered the nonlinear regime, and one would expect the growth to be slowing down relative to linear predictions. As stated, this could be due to a breakdown of the constant velocity assumption or the influence of modest RT growth coupling to the RM process.

Two dimensional simulations were performed using a combination of the GORGON MHD code and the xRAGE radiation

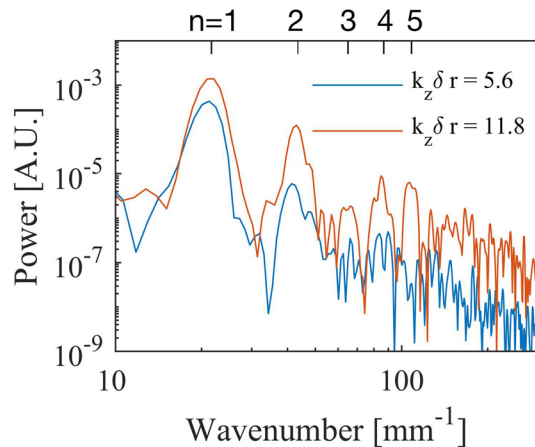


FIG. 9. Fourier transforms of the contours obtained from experiment z3244. t_1 is shown in blue corresponding to a displacement $k_z \delta r = 5.6$ and t_2 is shown in orange corresponding to $k_z \delta r = 11.8$.

hydrodynamics code. GORGON is used to model the drive of the liner through peak current, evolving the instabilities on the outer surface in a manner that has been shown to be consistent with previous experiments.^{35,45} For this portion of the calculation, a three dimensional Eulerian grid with $30 \mu\text{m}$ resolution was used with no strength model, tabulated Sesame equations of state, and electrical conductivities based on LMD and DFT. At a point shortly before the shock impacts the rod, all of the hydrodynamic information from GORGON is linked to xRAGE in 2D cylindrical geometry, eliminating the electromagnetic fields, using the RageRunner tool. From this point on, the liner and shock dynamics proceed ballistically. Since all of the dynamics of interest occur after peak current, when the majority of the drive energy has already been delivered, and because we have shown magnetic fields in

the vicinity of the rod are negligible, this paradigm is well suited to modeling this experiment. Shown are simulations using three levels of adaptive mesh refinement (AMR) in xRAGE to resolve the perturbation to $3.73 \mu\text{m}$ resolution (a convergence study ran to four levels of AMR, $1.86 \mu\text{m}$ resolution, and found that the large scales of the perturbation were already resolved at this level). The same tabulated equations of state were used as in the GORGON calculation and no strength models were used as the rod is melted by the shock. This formalism leverages the strengths of each of these tools that have been developed and exercised against experiments for years without requiring lengthy development and benchmarking of new tools. Figures 10(a) and 10(b) show density plots from the xRAGE simulation at times corresponding to the images from experiment z3244 (Figs. 4(c) and 4(e), respectively).

The xRAGE simulation reproduces the interface position, shock position, and perturbation amplitude well at both times. The experimental perturbation profiles and shock locations are shown in red for comparison. The details of the perturbation shape are not reproduced exactly (xRAGE predicts more high-mode structure), but the overall amplitude agrees extremely well. The mode growth is extracted from these simulations and shown in Fig. 8 as the dashed line. The agreement between experiment and simulation is quite good at all times, and better than the theory. The initial compression of the perturbation is also in good agreement with our simple estimate. The precipitous rollover of the instability amplitude seen in the calculation suggests that the nonlinear behavior of the mode is likely due to convergence effects after all. The simulation shows that at this time, in agreement with experiments, the shock has not restructured the interface. However, the pressure is rising dramatically due to the high degree of convergence. This is shown in Fig. 10(c) where the pressure (solid lines) and velocity (dashed lines) are shown for the bubble (blue) and spike (orange) tips as a function of time. The vertical black lines mark the times corresponding to the two images in (a) and (b). It is apparent that the bubble tips are experiencing this rise in pressure sooner and

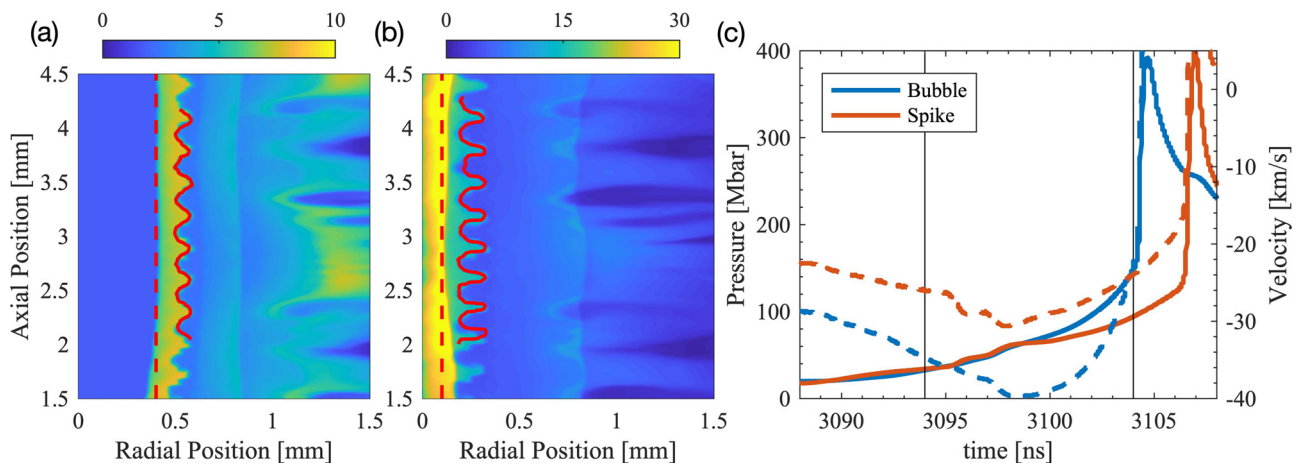


FIG. 10. (a) Density plot from the xRAGE simulation at the time corresponding to the image recorded on z3244 t_1 [shown in Fig. 4(c)]. (b) Density plot from the xRAGE simulation at the time corresponding to the image recorded on z3244 t_2 [shown in Fig. 4(e)]. The solid red lines show the experimentally measured perturbation at each time. The vertical dashed lines show the experimentally measured mean shock location at each time. Colorbars above (a) and (b) represent the material density in g/cm^3 . (c) Pressure (solid lines) and radial velocity (dashed lines) from the xRAGE simulation for tracers placed at the bubble (blue) and spike (orange) tips. Vertical black lines correspond to the times at which the images were taken.

more dramatically than the spikes, again due to convergence effects. This asymmetry is causing the bubbles to effectively slow down and become flatter, giving rise to the higher order harmonics. This deceleration can be seen in the velocity traces, both of which turn upward at ~ 3098 ns, marking a deceleration of the interface due to increasing back pressure. The bubble, however, experiences a much more dramatic deceleration than the spike. This phase corresponds to a time when the RM process is being directly modified by convergence effects. Finally, the sharp vertical rise in each of the traces corresponds to the time at which the reflected shock impacts the perturbation. There is a ~ 2.5 ns delay between when the bubble and spike experience this reshock.

IV DISCUSSION AND FUTURE WORK

In this work, we have established the use of cylindrical compression by magnetic fields as a powerful tool in studying hydrodynamic instabilities in the HED regime. The energy provided by the use of the Z pulsed power generator to perform the compression affords several distinct advantages including the following: (1) Pulsed power eliminates hot electron preheat caused by high power lasers, (2) it enables the use of large samples and wavelengths that can be highly resolved with available diagnostics, and (3) it affords the use of solid and liquid materials eliminating the need for foams and precision machining of interfaces. Additionally, the cylindrical geometry provides a natural reshock as well as the ability to perform Abel inversions to obtain the local material density. With regard to item (2), the radiography diagnostic used in this study provides a large field of view (~ 4 mm) with a high spatial resolution of ~ 12 μm . The perturbation wavelength of 300 μm affords the ability to measure a large number of wavelengths within this field of view, providing high confidence observation of high harmonics in the non-linear growth phase. We observed the presence of the fifth harmonic of the seeded mode, corresponding to a wavelength of 60 μm , which is still well resolved. By contrast, laser driven planar platforms on the NIF typically achieve a spatial resolution of ~ 25 μm using a large area backlighter and pinhole array.¹¹ Recent work has implemented a crystal imager similar to that used in this study to achieve higher spatial resolution⁴⁶ although the target dimensions and field of view provided in this system are substantially smaller than those provided by these experiments.

In order to compare these experiments with high fidelity simulations, a link was developed between the GORGON MHD code and the xRAGE radiation hydrodynamics code. This capability, called RageRunner, is well suited to modeling these experiments. The measured perturbation amplitude is compared with both 1D theory and the 2D calculations. Only the 2D calculations show that the late time non-linear growth is likely modified by convergence effects as the bubbles experience a higher back-pressure than the spikes. Detailed analysis of the simulations show that the bubbles experience an onset of back pressure and associated deceleration more severely and before the spikes do. This results in a flattening of the bubbles relative to the spikes and associated growth of higher order harmonics. The excellent agreement between experiment and simulation at the measurement times supports this conclusion.

Future work on this platform will focus on improving the stability of the liner so that measurements can be made later in time at higher convergence and after the interface is reshocked. We will also explore the use of multiple wavelengths to increase the amount of data

obtained on a single shot. The reshock phase is a particularly interesting area of future study. Simulations predict a relatively long, ~ 20 ns, dwell time after re-shock where the interface is approximately stationary and the perturbation continues to evolve before disassembly occurs. This will provide an opportunity to study instability-driven mixing between the fluids at high energy density and with convergence effects over ~ 40 ns drive times. Finally, the large energy available and flexibility of pulsed power drive enables us to explore the use of nested cylinders, azimuthal modes, and 3D helical modes, all of which are currently being considered.

ACKNOWLEDGMENTS

Sandia National Laboratories is a multission laboratory managed and operated by National Technology & Engineering Solutions of Sandia, LLC, a wholly owned subsidiary of Honeywell International Inc., for the U.S. Department of Energy's National Nuclear Security Administration under contract DE-NA0003525. This paper describes objective technical results and analysis. Any subjective views or opinions that might be expressed in the paper do not necessarily represent the views of the U.S. Department of Energy or the United States Government. Portions of this work were funded by Los Alamos National Laboratory operating under contract 89233218CNA000001 with Triad National Security LLC and by the Krell Institute via the Stewardship Science Graduate Fellowship through Grant No. DE-NA0003864. Raw data were generated at the Sandia National Laboratories' Z Machine. Derived data supporting the findings of this study are available within the article.

REFERENCES

- ¹J. Kane, R. P. Drake, and B. A. Remington, "An evaluation of the Richtmyer-Meshkov instability in supernova remnant formation," *Astrophysical J.* **511**, 335–340 (1999).
- ²J. Matsumoto and Y. Masada, "Rayleigh-Taylor and Richtmyer-Meshkov instabilities in relativistic hydrodynamic jets," *EPJ Web Conf.* **61**, 02005 (2013).
- ³S. Atzeni and J. M. ter Vehn, *The Physics of Inertial Fusion*, 1st ed. (Oxford University Press, 2004), p. 19.
- ⁴R. Richtmyer, "Taylor instability in shock acceleration of compressible fluids," *Commun. Pure Appl. Math.* **13**, 297–319 (1960).
- ⁵E. Meshkov, "Instability of the interface of two gases accelerated by a shock wave," *Fluid Dyn.* **4**, 101–104 (1972).
- ⁶K. Nishihara, J. G. Wouchuk, C. Matsuoka, R. Ishizaki, and V. V. Zhakhovsky, "Richtmyer-meshkov instability: Theory of linear and nonlinear evolution," *Philos. Trans. Roy. Soc. A* **368**, 1769–1807 (2010).
- ⁷G. I. Taylor, "The formation of a blast wave by a very intense explosion i. theoretical discussion," *Proc. R. Soc. London, Ser. A* **201**, 159–174 (1950).
- ⁸F. W. Doss, J. L. Kline, K. A. Flippo, T. S. Perry, B. G. DeVolder, I. Tregillis, E. N. Loomis, E. C. Merritt, T. J. Murphy, L. Welser-Sherrill, and J. R. Fincke, "The shock/shear platform for planar radiation-hydrodynamics experiments on the national ignition facility," *Phys. Plasmas* **22**, 056303 (2015).
- ⁹K. A. Flippo, F. W. Doss, E. C. Merritt, B. G. DeVolder, C. A. Di Stefano, P. A. Bradley, D. Capelli, T. Cardenas, T. R. Desjardins, F. Fierro, C. M. Huntington, J. L. Kline, L. Kot, S. Kurien, E. N. Loomis, S. A. MacLaren, T. J. Murphy, S. R. Nagel, T. S. Perry, R. B. Randolph, A. Rasmus, and D. W. Schmidt, "Late-time mixing and turbulent behavior in high-energy-density shear experiments at high atwood numbers," *Phys. Plasmas* **25**, 056315 (2018).
- ¹⁰T. Desjardins, C. Di Stefano, T. Day, D. Schmidt, E. Merritt, F. Doss, K. Flippo, T. Cardenas, B. DeVolder, P. Donovan, S. Edwards, F. Fierro, R. Gonzales, L. Goodwin, C. Hamilton, T. Quintana, R. Randolph, A. Rasmus, T. Sedillo, C. Wilson, and L. Welser-Sherrill, "A platform for thin-layer Richtmyer-Meshkov at omega and the nif," *High Energy Density Phys.* **33**, 100705 (2019).

- ¹¹S. R. Nagel, K. S. Raman, C. M. Huntington, S. A. MacLaren, P. Wang, M. A. Barrios, T. Baumann, J. D. Bender, L. R. Benedetti, D. M. Doane, S. Felker, P. Fitzsimmons, K. A. Flippo, J. P. Holder, D. N. Kaczala, T. S. Perry, R. M. Seugling, L. Savage, and Y. Zhou, "A platform for studying the Rayleigh–Taylor and Richtmyer–Meshkov instabilities in a planar geometry at high energy density at the national ignition facility," *Phys. Plasmas* **24**, 072704 (2017).
- ¹²C. C. Kuranz, H. S. Park, C. M. Huntington, A. R. Miles, B. A. Remington, T. Plewa, M. R. Trantham, H. F. Robey, D. Shvarts, A. Shimony, K. Raman, S. MacLaren, W. C. Wan, F. W. Doss, J. Kline, K. A. Flippo, G. Malamud, T. A. Handy, S. Prisbrey, C. M. Krauland, S. R. Klein, E. C. Harding, R. Wallace, M. J. Grosskopf, D. C. Marion, D. Kalantar, E. Giraldez, and R. P. Drake, "How high energy fluxes may affect rayleigh–taylor instability growth in young supernova remnants," *Nat. Commun.* **9**, 1564 (2018).
- ¹³C. A. Di Stefano, G. Malamud, C. C. Kuranz, S. R. Klein, C. Stoeckl, and R. P. Drake, "Richtmyer–Meshkov evolution under steady shock conditions in the high-energy-density regime," *Appl. Phys. Lett.* **106**, 114103 (2015).
- ¹⁴C. D. Stefano, G. Malamud, C. Kuranz, S. Klein, and R. Drake, "Measurement of Richtmyer–Meshkov mode coupling under steady shock conditions and at high energy density," *High Energy Density Phys.* **17**, 263–269 (2015).
- ¹⁵W. W. Hsing and N. M. Hoffman, "Measurement of feedthrough and instability growth in radiation-driven cylindrical implosions," *Phys. Rev. Lett.* **78**, 3876–3879 (1997).
- ¹⁶J. R. Fincke, N. E. Lanier, S. H. Batha, R. M. Hueckstaedt, G. R. Magelssen, S. D. Rothman, K. W. Parker, and C. J. Horsfield, "Postponement of saturation of the Richtmyer–Meshkov instability in a convergent geometry," *Phys. Rev. Lett.* **93**, 115003 (2004).
- ¹⁷K. Parker, C. J. Horsfield, S. D. Rothman, S. H. Batha, M. M. Balkey, N. D. Delamater, J. R. Fincke, R. M. Hueckstaedt, N. E. Lanier, and G. R. Magelssen, "Observation and simulation of plasma mix after reshock in a convergent geometry," *Phys. Plasmas* **11**, 2696–2701 (2004).
- ¹⁸J. P. Sauppe, S. Palaniyappan, B. J. Tobias, J. L. Kline, K. A. Flippo, O. L. Landen, D. Shvarts, S. H. Batha, P. A. Bradley, E. N. Loomis, N. N. Vazirani, C. F. Kawaguchi, L. Kot, D. W. Schmidt, T. H. Day, A. B. Zylstra, and E. Malka, "Demonstration of scale-invariant Rayleigh–Taylor instability growth in laser-driven cylindrical implosion experiments," *Phys. Rev. Lett.* **124**, 185003 (2020).
- ¹⁹M. E. Savage, K. R. LeChien, M. R. Lopez, B. S. Stoltzfus, W. A. Stygar, D. S. Artery, J. A. Lott, and P. A. Corcoran, "Status of the z pulsed power driver," in *2011 IEEE Pulsed Power Conference* (IEEE, 2011) pp. 983–990.
- ²⁰M. L. Spaeth, K. R. Manes, D. H. Kalantar, P. E. Miller, J. E. Heebner, E. S. Bliss, D. R. Spec, T. G. Parham, P. K. Whitman, P. J. Wegner, P. A. Baisden, J. A. Menapace, M. W. Bowers, S. J. Cohen, T. I. Suratwala, J. M. D. Nicola, M. A. Newton, J. J. Adams, J. B. Trenholme, R. G. Finucane, R. E. Bonanno, D. C. Rardin, P. A. Arnold, S. N. Dixit, G. V. Erbert, A. C. Erlandson, J. E. Fair, E. Feigenbaum, W. H. Gourdin, R. A. Hawley, J. Honig, R. K. House, K. S. Jancaitis, K. N. LaFortune, D. W. Larson, B. J. L. Galloudec, J. D. Lindl, B. J. McGowan, C. D. Marshall, K. P. McCandless, R. W. McCracken, R. C. Montesanti, E. I. Moses, M. C. Nostrand, J. A. Pryatel, V. S. Roberts, S. B. Rodriguez, A. W. Rowe, R. A. Sacks, J. T. Salmon, M. J. Shaw, S. Sommer, C. J. Stolz, G. L. Tietbohl, C. C. Widmayer, and R. Zacharias, "Description of the nif laser," *Fusion Sci. Technol.* **69**, 25–145 (2016).
- ²¹T. Boehly, D. Brown, R. Craxton, R. Keck, J. Knauer, J. Kelly, T. Kessler, S. Kumpan, S. Loucks, S. Letzring, F. Marshall, R. McCrory, S. Morse, W. Seka, J. Soures, and C. Verdon, "Initial performance results of the omega laser system," *Opt. Commun.* **133**, 495–506 (1997).
- ²²A. C. Robinson and C. J. Garasi, "Three-dimensional z-pinch wire array modeling with alegra-hedp," *Comput. Phys. Commun.* **164**, 408–413 (2004).
- ²³J. P. Chittenden, S. V. Lebedev, C. A. Jennings, S. N. Bland, and A. Ciardi, "X-ray generation mechanisms in three-dimensional simulations of wire array z-pinch," *Plasma Phys. Controlled Fusion* **46**, B457–B476 (2004).
- ²⁴M. Gittings, R. Weaver, M. Clover, T. Betlach, N. Byrne, R. Coker, E. Dendy, R. Hueckstaedt, K. New, W. R. Oakes, D. Ranta, and R. Stefan, "The RAGE radiation-hydrodynamic code," *Comput. Sci. Discovery* **1**, 015005 (2008).
- ²⁵S. A. Slutz, M. C. Herrmann, R. A. Vesey, A. B. Sefkow, D. B. Sinars, D. C. Rovang, K. J. Peterson, and M. E. Cuneo, "Pulsed-power-driven cylindrical liner implosions of laser preheated fuel magnetized with an axial field," *Phys. Plasmas* **17**, 056303 (2010).
- ²⁶M. R. Gomez, S. A. Slutz, A. B. Sefkow, D. B. Sinars, K. D. Hahn, S. B. Hansen, E. C. Harding, P. F. Knapp, P. F. Schmit, C. A. Jennings, T. J. Awe, M. Geissel, D. C. Rovang, G. A. Chandler, G. W. Cooper, M. E. Cuneo, A. J. Harvey-Thompson, M. C. Herrmann, M. H. Hess, O. Johns, D. C. Lamppa, M. R. Martin, R. D. McBride, K. J. Peterson, J. L. Porter, G. K. Robertson, G. A. Rochau, C. L. Ruiz, M. E. Savage, I. C. Smith, W. A. Stygar, and R. A. Vesey, "Experimental demonstration of fusion-relevant conditions in magnetized liner inertial fusion," *Phys. Rev. Lett.* **113**, 155003 (2014).
- ²⁷P. F. Knapp, M. R. Martin, D. H. Dolan, K. Cochrane, D. Dalton, J.-P. Davis, C. A. Jennings, G. P. Loisel, D. H. Romero, I. C. Smith, E. P. Yu, M. R. Weis, T. R. Mattsson, R. D. McBride, K. Peterson, J. Schwarz, and D. B. Sinars, "Direct measurement of the inertial confinement time in a magnetically driven implosion," *Phys. Plasmas* **24**, 042708 (2017).
- ²⁸P. F. Schmit, P. F. Knapp, S. B. Hansen, M. R. Gomez, K. D. Hahn, D. B. Sinars, K. J. Peterson, S. A. Slutz, A. B. Sefkow, T. J. Awe, E. Harding, C. A. Jennings, G. A. Chandler, G. W. Cooper, M. E. Cuneo, M. Geissel, A. J. Harvey-Thompson, M. C. Herrmann, M. H. Hess, O. Johns, D. C. Lamppa, M. R. Martin, R. D. McBride, J. L. Porter, G. K. Robertson, G. A. Rochau, D. C. Rovang, C. L. Ruiz, M. E. Savage, I. C. Smith, W. A. Stygar, and R. A. Vesey, "Understanding fuel magnetization and mix using secondary nuclear reactions in magneto-inertial fusion," *Phys. Rev. Lett.* **113**, 155004 (2014).
- ²⁹P. F. Knapp, P. F. Schmit, S. B. Hansen, M. R. Gomez, K. D. Hahn, D. B. Sinars, K. J. Peterson, S. A. Slutz, A. B. Sefkow, T. J. Awe, E. Harding, C. A. Jennings, M. P. Desjarlais, G. A. Chandler, G. W. Cooper, M. E. Cuneo, M. Geissel, A. J. Harvey-Thompson, J. L. Porter, G. A. Rochau, D. C. Rovang, C. L. Ruiz, M. E. Savage, I. C. Smith, W. A. Stygar, and M. C. Herrmann, "Effects of magnetization on fusion product trapping and secondary neutron spectra," *Phys. Plasmas* **22**, 056312 (2015).
- ³⁰P. K. Rambo, I. C. Smith, J. L. Porter, Jr., M. J. Hurst, C. S. Speas, R. G. Adams, A. J. Garcia, E. Dawson, B. D. Thurston, C. Wakefield, J. W. Kellogg, M. J. Slattery, H. C. Ives III, R. S. Broyles, J. A. Caird, A. C. Erlandson, J. E. Murray, W. C. Behrendt, N. D. Neilsen, and J. M. Narduzzi, "Z-beamlet: A multikilojoule, terawatt-class laser system," *Appl. Opt.* **44**, 2421–2430 (2005).
- ³¹M. S. Schollmeier, P. F. Knapp, D. J. Ampleford, E. C. Harding, C. A. Jennings, D. C. Lamppa, G. P. Loisel, M. R. Martin, G. K. Robertson, J. E. Shores, I. C. Smith, C. S. Speas, M. R. Weis, J. L. Porter, and R. D. McBride, "A 7.2 keV spherical x-ray crystal backlighter for two-frame, two-color backlighting at sandia's z pulsed power facility," *Rev. Sci. Instrum.* **88**, 103503 (2017).
- ³²R. W. Lemke, M. D. Knudson, D. E. Bliss, K. Cochrane, J.-P. Davis, A. A. Giunta, H. C. Harjes, and S. A. Slutz, "Magnetically accelerated, ultrahigh velocity flyer plates for shock wave experiments," *J. Appl. Phys.* **98**, 073530 (2005).
- ³³J.-P. Davis, C. Deeney, M. D. Knudson, R. W. Lemke, T. D. Pointon, and D. E. Bliss, "Magnetically driven isentropic compression to multimegabar pressures using shaped current pulses on the z accelerator," *Phys. Plasmas* **12**, 056310 (2005).
- ³⁴J.-P. Davis and M. D. Knudson, "Multi-megabar measurement of the principal quasi-isentrope for tantalum," *AIP Conf. Proc.* **1195**, 673–676 (2009).
- ³⁵R. D. McBride, M. R. Martin, R. W. Lemke, J. B. Greenly, C. A. Jennings, D. C. Rovang, D. B. Sinars, M. E. Cuneo, M. C. Herrmann, S. A. Slutz, C. W. Nakhleh, D. D. Ryutov, J.-P. Davis, D. G. Flicker, B. E. Blue, K. Tomlinson, D. Schroen, R. M. Stamm, G. E. Smith, J. K. Moore, T. J. Rogers, G. K. Robertson, R. J. Kamm, I. C. Smith, M. Savage, W. A. Stygar, G. A. Rochau, M. Jones, M. R. Lopez, J. L. Porter, and M. K. Matzen, "Beryllium liner implosion experiments on the z accelerator (unpublished) for magnetized liner inertial fusion," *Phys. Plasmas* **20**, 056309 (2013).
- ³⁶J. D. J. S. P. Lyon, "Sesame: The Los Alamos National Laboratory equation of state database," Report No. LA-UR-92-3407, 1992.
- ³⁷J. Cheung and N. W. Ashcroft, "Resistivity of liquid metals under elevated pressure," *Phys. Rev. B* **18**, 559–568 (1978).
- ³⁸J. Cheung and N. W. Ashcroft, "Aluminum under high pressure. II—Resistivity," *Phys. Rev. B* **20**, 2991–2998 (1979).
- ³⁹M. P. Desjarlais, J. D. Kress, and L. A. Collins, "Electrical conductivity for warm, dense aluminum plasmas and liquids," *Phys. Rev. E* **66**, 025401 (2002).
- ⁴⁰M. Desjarlais, "Practical improvements to the lee-more conductivity near the metal-insulator transition," *Contrib. Plasma Phys.* **41**, 267–270 (2001).

- ⁴¹R. F. Chisnell, "An analytic description of converging shock waves," *J. Fluid Mech.* **354**, 357–375 (1998).
- ⁴²M. Lombardini and D. I. Pullin, "Small-amplitude perturbations in the three-dimensional cylindrical richtmyer–meshkov instability," *Phys. Fluids* **21**, 114103 (2009).
- ⁴³A. L. Velikovich and G. Dimonte, "Nonlinear perturbation theory of the incompressible Richtmyer-Meshkov instability," *Phys. Rev. Lett.* **76**, 3112–3115 (1996).
- ⁴⁴A. L. Velikovich, M. Herrmann, and S. I. Abarzhi, "Perturbation theory and numerical modelling of weakly and moderately nonlinear dynamics of the incompressible Richtmyer-Meshkov instability," *J. Fluid Mech.* **751**, 432–479 (2014).
- ⁴⁵R. D. McBride, S. A. Slutz, C. A. Jennings, D. B. Sinars, M. E. Cuneo, M. C. Herrmann, R. W. Lemke, M. R. Martin, R. A. Vesey, K. J. Peterson, A. B. Sefkow, C. Nakhleh, B. E. Blue, K. Killebrew, D. Schroen, T. J. Rogers, A. Laspe, M. R. Lopez, I. C. Smith, B. W. Atherton, M. Savage, W. A. Stygar, and J. L. Porter, "Penetrating radiography of imploding and stagnating beryllium liners on the z accelerator," *Phys. Rev. Lett.* **109**, 135004 (2012).
- ⁴⁶G. N. Hall, C. M. Krauland, M. S. Schollmeier, G. E. Kemp, J. G. Buscho, R. Hibbard, N. Thompson, E. R. Casco, M. J. Ayers, S. L. Ayers, N. B. Meezan, L. F. B. Hopkins, R. Nora, B. A. Hammel, L. Masse, J. E. Field, D. K. Bradley, P. Bell, O. L. Landen, J. D. Kilkenny, D. Mariscal, J. Park, T. J. McCarville, R. Lowe-Webb, D. Kalantar, T. Kohut, and K. Piston, "The crystal backlighter imager: A spherically bent crystal imager for radiography on the national ignition facility," *Rev. Sci. Instrum.* **90**, 013702 (2019).